Heliyon 10 (2024) e25271

Contents lists available at ScienceDirect

Heliyon

journal homepage: www.cell.com/heliyon

Research article

# Investigating the kinetics of layer development during the color etching of low-carbon steel with in-situ spectroscopic ellipsometry

József Bálint Renkó [a], Alekszej Romanenko [b,c], Tamás Bíró [a], Péter János Szabó [a], Péter Petrik [b,e], Attila Bonyár [d,*]

[a] Department of Materials Science and Engineering, Faculty of Mechanical Engineering, Budapest University of Technology and Economics, H-1111, Budapest, Bertalan Lajos street 7, Hungary
[b] Institute of Technical Physics and Materials Science, Centre for Energy Research, Konkoly Thege Str. 29-33, 1121, Budapest, Hungary
[c] Doctoral School of Chemistry, Eötvös Loránd University, Pázmány Péter sétány 1/A, 1117, Budapest, Hungary
[d] Department of Electronics Technology, Faculty of Electrical Engineering and Informatics, Budapest University of Technology and Economics, H-1111, Budapest, Egry József street 18, Hungary
[e] Department of Electrical Engineering, Institute of Physics, Faculty of Science and Technology, University of Debrecen, 4032, Debrecen, Hungary

ARTICLE INFO

*Keywords:*
In-situ
Color etching
Beraha−I
Optical microscopy
Spectroscopic ellipsometry
Layer development kinetics

ABSTRACT

Color etching is a useful corrosive process, widely applied in metallography to study the microstructure of metals. To prove the existence of the previously hypothesized steady-state etching rate, in-situ investigations were performed with spectroscopic ellipsometry during the color etching of ferritic materials. Kinetic information regarding the refractive index, extinction coefficient, and layer thickness were used to calculate the steady-state layer buildup rate, which was 1.90 ± 0.15 nm/s for low-carbon steel and 0.99 ± 0.06 nm/s for cast iron owing to its better corrosion resistance. The presented methodology and findings could help understanding other processes that involve the development of layers on metallic surfaces.

## 1. Introduction

In metallography, etching processes are standard tools to develop microstructure [1,2]. During etching, the previously polished surface reacts with the applied chemical and reveals certain parts of its structure depending on the nature of the applied etchant. As a result, grain boundaries, precipitations, and different phases or grains become visible while allowing further surface analysis [3,4]. Depending on the type of chemical reaction, etchants can be categorized as follows. Etchants, which merely dissolve the substrate's surface, belong to chemical etchants [5]. This process is highly selective and makes different textures visible by attacking only grain boundaries or certain phases. Usually, it contains no additional information other than revealing microstructure for metallographic examination. The second group includes etchants, which not only corrode and dissolve the substrate but also develop a mixture of compounds on its surface. They usually react directly with the grains instead of the grain boundaries. The resulting layer is primarily transparent, and as it grows, it results in a cyclic color change according to the interference criterion [6]. As the corrosion process continues, the layer loses its color (becomes uniformly dark brown) but stopping the process in its initial phase could provide additional information about phases, crystal structure, and grain orientation. This etching second group got its name after the resulting colorful grains and called color etchants. Although the range of applications is relatively wide for different etchants, there have been

* Corresponding author.
*E-mail address:* bonyar.attila@vik.bme.hu (A. Bonyár).

https://doi.org/10.1016/j.heliyon.2024.e25271
Received 21 November 2023; Received in revised form 2 January 2024; Accepted 23 January 2024
Available online 27 January 2024

only a few efforts to understand the kinetics of the etching process, especially for color etchants. In some cases, the chemical reactions were (at least partly) revealed, but etchants are used primarily out of habit without a proper understanding of the kinetics of the ongoing chemical reaction [7,8]. In addition, these studies focused specifically on the kinetics of etching of organic compounds or semiconductor materials but never on metallographically inspected alloys [9,10].

Though the related literature for alloys is insufficient for color etchants, an initial hypothesis could be formed about the etching kinetics. In 2019 a study was made to use the layer orientation dependency of color etching with Beraha–I on spheroidal cast iron to determine the crystallographic orientation of randomly selected ferrite grains [11]. This article laid the foundations of a new orientation determination method, which could determine orientation within the accuracy of 3° compared to electron backscatter diffractometry (EBSD). The presented model described a hypothesis about the kinetics of layer development based on the elapsed time between the extrema on the normalized intensity curves of the reflected light. In-situ examination of the color etching process allows for recording the color change of various grains on the selected area. Using these records, the normalized intensity curves for any given wavelength can be determined for each grain, showing that they have a cosine-like behavior with a declining amplitude, as seen in Fig. 1.

Although grains with different orientations have shifted curves compared to one another, due to the nature of normalized curves, the extrema of these curves imply to have the exact layer thickness according to the interference criteria (Eqs. (1) and (2)), only the required time to reach it will differ [12].

$$2n(\lambda)d\cos(\varphi) = \left(m - \frac{1}{2}\right)\lambda \tag{1}$$

$$2n(\lambda)d\cos(\varphi) = m\lambda \tag{2}$$

Considering any chosen wavelength ($\lambda$) in consecutive extrema, the growth of the product of layer thickness ($d$) and refractive index ($n$) will grow linearly as $m$ (the order of interference) increasing. Thus, without knowing the layer thickness or refractive index, we can conclude the ongoing layer development by analyzing the elapsed time between consecutive extrema. Using this technique, the study from 2019 described the kinetics using a resulting normalized intensity curve as follows.

First, based on the interference criteria, the existence of a constant etching speed was assumed, meaning the elapsed half-cycle time between intensity extrema should be the same ($t_{hc}$). Unfortunately, at the beginning of the etching, the substrate and the etchant have no direct connection due to the oxide layer on the substrate's surface. The etchant needs a small but measurable amount of time ($t_{oxide}$) to break through. Thus, the time required to reach the first minimum will be greater than the half-cycle time measured later, in other words, the etching rate ($v(t)$) is slower in this region. After the effect of the oxide layer is gone, a fast chemical reaction occurs. The reaction creates a thin nanometer size layer, a mixture of Beraha–I and the dissolved ferrite. The layer again separates the substrate from the etchant, meaning the etchant must diffuse through the layer to reach the substrate. As the process progresses and the layer grows, a slight but continuous decrease in etching speed can be observed (as can be seen in the appearance of $t_{lag}$). For the first couple of extrema ($t_{min}$, $t_{max}$), the decline was almost negligible; thus, the assumed constant cycle time (and constant etching rate $v_{const}$), could be determined. Leaving the zone of "steady-state etching", the reaction speed started dropping significantly. After the layer reached a certain thickness, the time required for the etchant to react with the surface increased so much that it practically stopped the measurable layer development.

As mentioned earlier, the refractive index and layer thickness should be directly measured during the process to prove the model. Unfortunately, the layer thickness was determined only ex-situ with atomic force microscopy (AFM), and the refractive index – which was wrongfully assumed constant for the whole surface at that time – was later calculated from the fitting function of the etching half-

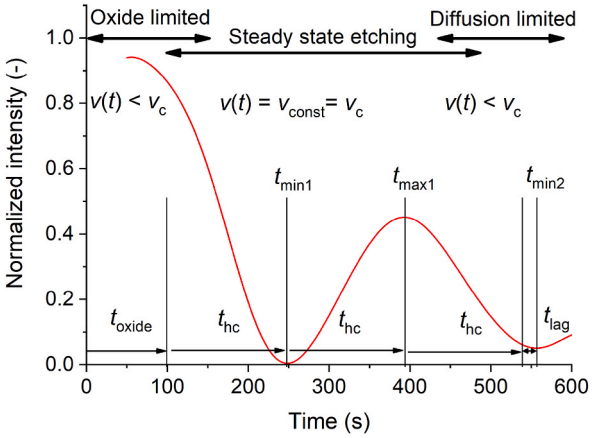


**Fig. 1.** The functional kinetics model with different regions for etching, based on the normalized intensity curve (red component) measured on a ferrite grain of the cast iron specimen (reproduced with permission, copyright: Elsevier, 2019 [11]). (For interpretation of the references to color in this figure legend, the reader is referred to the Web version of this article.)

cycle time between extrema on the normalized intensity curves. Due to these uncertainties, the measurement could neither achieve higher accuracy nor prove the hypothesis.

In 2022 another study on color etching showed that layer development is even more complex than expected [13]. Ex-situ analysis with a spectroscopic ellipsometer (SE) was made on color-etched ferrite surfaces, proving that the distribution of both the refractive index and the layer thickness can be directly measured. In addition, X-ray photoelectron spectroscopy (XPS) showed that the developed layer has both an axial and a lateral inhomogeneity. This means that the refractive index differs not only on grains with different crystallographic orientations but also along the thickness of the individual grains. Although this study did not directly address etching kinetics, its results are essential to understand and later prove our model.

As the paper above showed, with spectroscopic ellipsometry, the opportunity is given to measure refractive index and layer thickness, only the proper tool is required to achieve in-situ examination. In this work, we aimed to create a new method for in-situ analysis of color etching with spectroscopic ellipsometry, which could help improve the previously assumed kinetics of layer development and deepen our understanding of the etching process.

## 2. Experimental

### 2.1. Materials and sample preparation

In our experiments, Beraha−I solution was used as a color etchant, similar to the above-presented studies. The etchant is a mixture of 3 g $K_2S_2O_5$, 10 g $Na_2S_2O_3$ and 100 ml distilled water, which was freshly mixed right before the experiments. Beraha−I reacts well with various materials, such as ferrite in cast iron and low-carbon steels or copper in different copper alloys [14,15]. Due to the lack of acidic components, the reaction speed is significantly slower than other reagents. This ensures the necessary time for in-situ examinations.

The 2019 paper used spheroidal cast iron as a sample containing multiple structures, such as ferrite, pearlite, and graphite. Beraha−I reacts with ferrite in both ferrite and pearlite microstructures, resulting in a complex color change on the surface [11]. Although spectroscopic ellipsometry is suitable for measuring nanometer-sized layers, the diameter of the smallest area examined at a time is 0.3 mm or higher, and the results will always show the mean of this area. Thus, multiple reacting microstructures in the same material could alter the results. To resolve this problem, DC01 low-carbon steel was chosen as a sample. DC01 contains only the ferrite phase, making it suitable to present the layer development kinetics and prove our theory. The chemical composition of DC01 was determined with a PMI-Master Sort optical emission spectrometer, and the results are shown in Table 1.

To eliminate the effect of any preliminary deformation and get a homogeneous grain structure, the low-carbon steel was heated up to 850 °C, then cooled on air, resulting in a fine ferritic structure. Then the sample was embedded into vinyl, providing a fixed geometry essential for the various experiments. The embedded sample was ground and polished. The final polishing step was performed with a 1 μm diamond suspension for 10 min, providing the necessary surface.

As presented in a 2021 study, DC01 is a proper choice for grain coarsening heat treatment, resulting in millimeter-sized grains. Although this would theoretically allow us to examine the layer development of only one grain at a time, the currently available microfluidic cell system for spectroscopic ellipsometry – which will be presented later – does not allow this yet, because the equipment does not make it possible to move the sample with the necessary precision and focusing on only one grain. Furthermore, if the average surface kinetics wants to be determined, a finer grain structure may be more beneficial, as it does not allow any favored directions to dominate and eventually alter the results. To make sure our material has a properly fine grain structure, a preliminary etching was made to determine the average grain size, around 10 μm.

### 2.2. Optical microscopy

For the real-time monitoring of the etching process with an optical microscope (OM), the setup presented in Fig. 2 was used. The embedded sample was put into a microfluidic cell assembled from a chemically bonded glass sheet and a polydimethylsiloxane (PDMS) part. The sample seals the structure from one direction and creates a small inner cavity through which the etchant can flow. At the same time, the sample can be observed throughout the glass sheet under the optical microscope. The change of the sample's surface was recorded with a computer directly connected to a DP72 digital camera with an LMPlan 20 × /0.40 long working distance lens. This setup was proved useful in multiple studies since 2019 to examine not only cast iron or low carbons steels but also industrial-grade copper [11,13,16].

The closed system makes it possible to in-situ examine the etching process in a precisely controlled environment. Since the inner cavity of the microfluidic cell is very small, only a small amount of etchant is required. In addition to that, due to the smaller distances, the reaction occurs at a higher speed between the etchant and the substrate. To continuously refresh the etchant, a syringe pump is connected to the inlet of the microfluidic cell with a silicon tube that not only fills the cell with the etchant but also ensures a constant,

**Table 1**
Chemical composition of DC01 ferritic steel in atomic%.

| Fe | C | Mn | Cr | Mo | Ni | Al | Co | Cu | Nb |
|---|---|---|---|---|---|---|---|---|---|
| 98.9 | 0.092 | 0.616 | 0.081 | 0.013 | 0.034 | 0.064 | 0.017 | 0.118 | 0.065 |

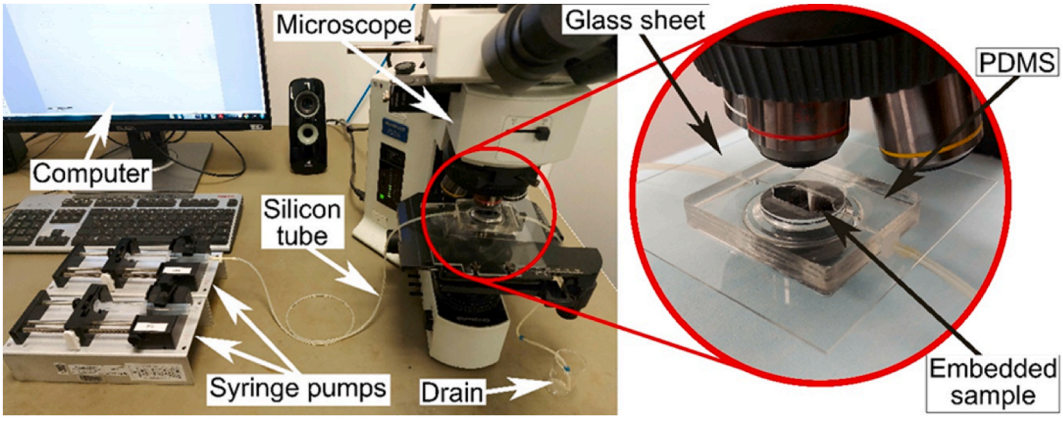


**Fig. 2.** Photograph of the measurement setup for the in situ optical microscopy investigations and the 3D design of the PDMS-based microfluidic cell with the embedded sample.

slow, and laminar flow (50 μl/min). The examination lasted for 550 s so that the domains of both oxide-limited etching, steady-state etching, and diffusion-limited etching could be determined later. Considering that the surface got over-etched around half of the process, the color change of the observed area is presented in Fig. 3 only for the first 180 s, from Fig. 3 a) to l).

### 2.3. Spectroscopic ellipsometry

A Woollam M-2000DI rotating compensator spectroscopic ellipsometer (SE) was used to determine $r_p/r_s = \tan(\Psi)\exp(i\Delta)$, where $r_p$ and $r_s$ are the complex reflection coefficients of light polarized parallel and perpendicular to the plane of incidence, respectively. The $\Psi$ and $\Delta$ spectra were acquired for 700 spectral points simultaneously in the wavelength range of 193–1690 nm. Due to the absorption of both the water and the glass cylinders, however, only the wavelength range between 445 and 1360 nm was used for the evaluation. The compensator rotates at 20 Hz, which, in ideal circumstances, would allow the determination of all the 2x700 spectral points within 50 msec. However, due to loss of intensity as the light travels through the experimental setup and reflects from the surface of the sample, a few times 10 or even 100 rotations are usually averaged to decrease the noise. The diameter of the light beam is approximately 3 mm without focusing, which is slightly decreased due to the geometric limitations of the microfluidic cell. The spot on the sample's surface is elongated depending on the angle of incidence.

For the in-situ observation of color etching with the spectroscopic ellipsometer, a special microfluidic cell was developed and

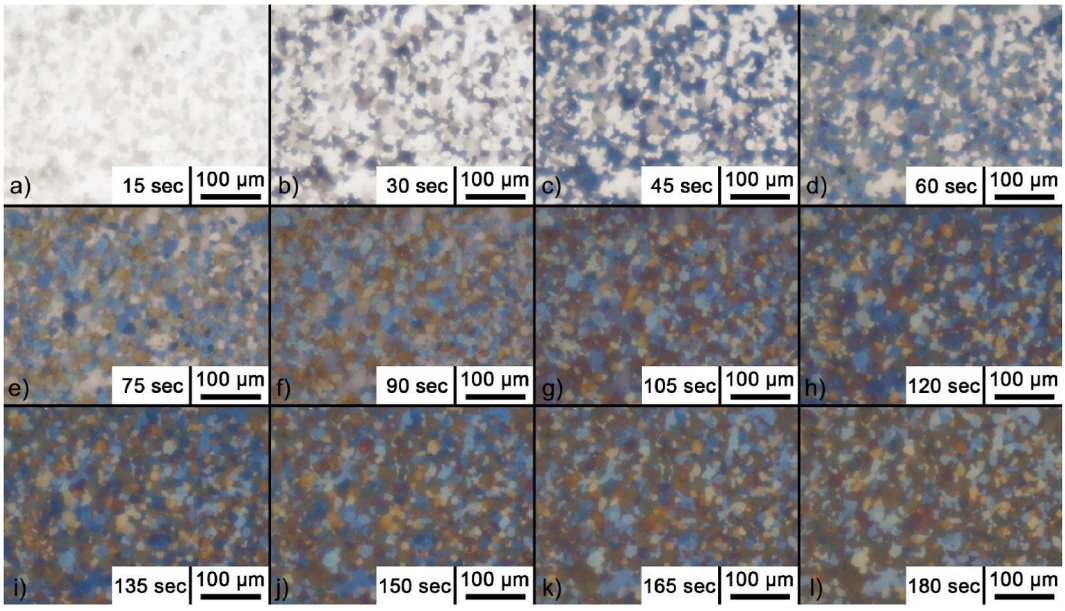


**Fig. 3.** Optical microscopic images from the investigated area of the specimen during the early stages of color etching. From a) to l) the etching time increases in 15 s intervals. (For interpretation of the references to color in this figure legend, the reader is referred to the Web version of this article.)

presented first in 2021 [17]. Similarly to the microfluidic cell designed for an optical microscope, this one can create a sealed cavity while protecting the SE from corrosion. Its modified construction closes the upper part of the PDMS cell (where in the previous model, the glass sheet was bonded) and replaces it with a 3 mm wide light path through which measurements with a spectroscopic ellipsometer can be performed. The advantage of this design is that the glass plates are placed perpendicularly in the light path, so the light source used for the examination can penetrate them without reflection. Thus, the loss during the process can be minimized, and the maximal light intensity can reach the detector from the sample's surface at the other side of the cell.

Due to the complex nature of this microfluidic system, some disadvantages must be taken into account, although the cell was designed specifically for SE. First, the glass plates closing the light path may not be perfectly perpendicular to the surface, which could cause a reasonable amount of intensity loss. Though this could be resolved by altering the angle of incidence for the measurements, it is fixed at 55° due to the geometry of the cell, and later it cannot significantly deviate from it (approx. ±5°). Second, the cell does not allow simultaneous optical inspection, so the precise positioning of the sample is impossible. The only way to visually follow and control the positioning is through the light path. This way, to record the change of only one grain, the sample must have a grain size bigger than the 3 mm diameter light path (preferably single crystals), ensuring nothing else is in the focus position. Otherwise, the measurement will always show the average of the examined area.

After assembling the setup and fixing the microfluidic cell to the worktable (Fig. 4), the ideal angle of incidence was determined by finding the maximal intensity on the detector and setting it to 53°, which is still comfortable in the available incidence range. As earlier described, the purpose of the measurements is to adequately describe the kinetics of layer development on the whole surface, thus, a small average grain size is rather suitable for the experiments. Consequently, neither the manufacturing inaccuracies nor the grain size is a problem in our case.

To reproduce the conditions of the previous measurement as good as possible during the etching process under SE, the known conditions were set to the same, such as the temperature (21 °C) and the etchant flow rate (50 μl/min), while the same mixture of Beraha−I was used for both experiments. The sample was repolished between measurements with the previously described method, and the area of interest was determined with high proximity based on the markings placed on the surface. The markings were close enough to identify the approximate area but far enough not to influence any measurement. It is important to mention that the measurements were not made on one single grain but rather the average of several grains due to the size of the light spot.

Despite the effort to create similar conditions in both microfluidic cells, the differences must also consider before comparing the two etching processes. The microfluidic cell for OM has a simple and symmetric cavity that ensures laminar flow during the process. This results in a slower but more controllable process with a continuously refreshed etchant. In contrast, the microfluidic cell for SE has a more complex, asymmetric geometry that requires significantly more etchant to fill its inner cavity. For a proper fill, a larger flow speed is necessary at the initial stage of the process. As a result, both the faster filling and the asymmetric construction may result in a turbulent flow.

Another factor to be considered is the filling medium of the cavity prior to the experiment. For the OM observation, the microfluidic cell was initially empty, thus, Beraha−I directly filled the cavity, replacing air. For the SE analysis, however, it was previously filled with distilled water as it was necessary to completely remove air bubbles stuck in the light path. This previous filling has multiple effects. First, considering that DC01 low-carbon steel has very poor corrosion resistance, the preliminary wetting of the surface could at least partially remove the oxide layer from the surface, allowing it to reach the steady-state etching faster. Second, the start and end of the etching could be determined less accurately, as the etchant will mix with distilled water, resulting in a fast but not immediate concentration change. To properly replace water with Beraha-I, the initial flow speed was increased to 1000 μl/min. The volume of the cavity in this microfluidic cell is approx. 90 $mm^3$, thus, the filling requires at least 6 s at this rate. Since the Beraha-I and distilled water have different refractive properties, a significant change in the detected light intensity indicates that the etchant reached the observed surface and the process started. After 10 s of that point, almost twice as much etchant was pumped through the system as the volume of the cavity, so the etchant flow rate was set back to 50 μl/min. To stabilize the developed layer at the end of the experiment, the Beraha-I

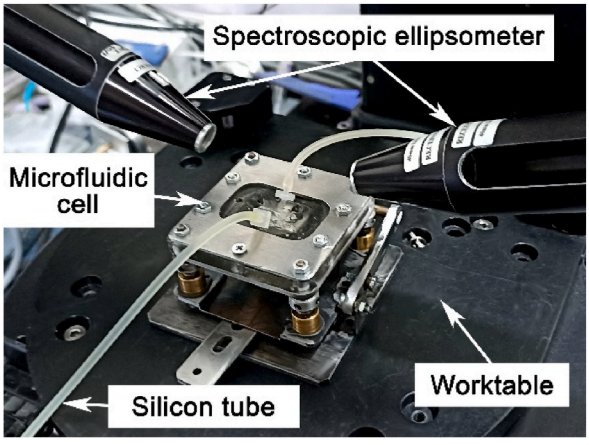


**Fig. 4.** Photograph of the measurement setup for the in-situ investigations with a spectroscopic ellipsometer.

was flushed out of the system with distilled water at an increased flow rate of 500 μl/min.

Finally, to avoid the over-etching of the surface during in-situ SE, the etching time was determined the following way. As later presented, the OM examination highlighted that it is important to monitor the intensity change and, if possible, stop the etching process between the first local minimum and maximum of luminance measured over the whole surface. The surface analysis of OM showed that the average luminance of low-carbon steel reached its first minimum of around 120 s. Considering this and the fact that during in-situ ellipsometry, the surface is hydrated prior to etching, the first intensity minimum is expected to be reached sooner. To minimize the chance of slipping through the first maximum, the approximated etching time was chosen for 120 s. It is long enough that even the slowest grains will reach their first minima but not long enough that any grain would be over-etched. The presented measurements will show the process as follows. The etching will start from the moment when the Beraha−I reaches the surface, as it results in a drastic refractive index change, separating the process from the initial state. After replacing the water, the etching was ongoing for 110 s (120 s total) before distilled water was infused into the cavity to stabilize the layer (another approx. 10 sec concentration shift). The rehydrated state was held for up to 150 s to stabilize the layer before the measurement was stopped.

## 3. Results and discussion

### 3.1. Image processing of the optical microscope results

The image processing of the optical microscope results contained two different experiments. First, 25 individual grains were selected to measure their intensity change for different wavelengths – namely red (R), green (G), and blue (B) – during the process (Fig. 5). By determining the local extrema of these curves, the characteristic times can be calculated, such as half-cycle time ($t_{hc}$), the necessary time for oxide breakthrough ($t_{oxide}$) at the beginning of the process, or the moment of over-etching ($t_{over}$). This would help decide how long of etching is required during SE not to over-etch the surface and to connect certain domains of OM and SE observations. Second, two larger areas (Fig. 5 area A and B) were selected, which would be used to compare the averaged intensity changes to one another and the etching rates calculated for OM and SE.

By analyzing the intensity change of the selected 25 grains, the observed cyclic color change occurs once or twice for each grain. First, they develop a light-brownish color that turns blue. Later, this will reach a brownish state again, although this time, a darker one. As the layer growth decreases due to the continuously increasing diffusion limitation, from around 300 s, grains will not only keep the same color, but they become less distinguishable from one another. From this point, the grains became over-etched. The corresponding intensity changes for a randomly selected grain (#2) are presented in Fig. 6.

The intensity of different light components could depend on various extrinsic factors, such as the direct light that illuminates the surface, the brightness of the environment, the time of day, or the reflective and light-absorbing ability of the surrounding surfaces. Due to these factors, the direct comparison and evaluation of intensity curves may not show a fully representative image of the surface area. To eliminate these differences, the normalized brightness (luminance) was calculated from the individual RGB components. By using luminance, different wavelength components are used at the same time, thus, a more general picture can be drawn about the surface. Moreover, SE can also measure light intensity, so it can also be utilized later for further comparison. In Eq. (3), $L$ represents the luminance, while $R$, $G$, and $B$ are the normalized intensity of red, green, and blue light components, respectively [18].

$$L = \sqrt{0.299 \bullet R^2 + 0.587 \bullet G^2 + 0.114 \bullet B^2} \tag{3}$$

By using luminance curves, the characteristic times were determined for each grain. First, the half-cycle ($t_{hc}$) time was calculated as

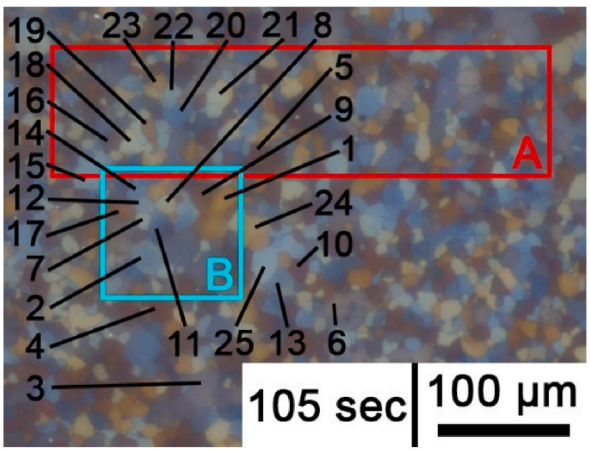


**Fig. 5.** Optical microscopic image with the selected 25 grains from the investigated area of the specimen during color etching at 105 s. The areas on which the average intensity curves were evaluated are shown with red (A) and turquoise (B). (For interpretation of the references to color in this figure legend, the reader is referred to the Web version of this article.)

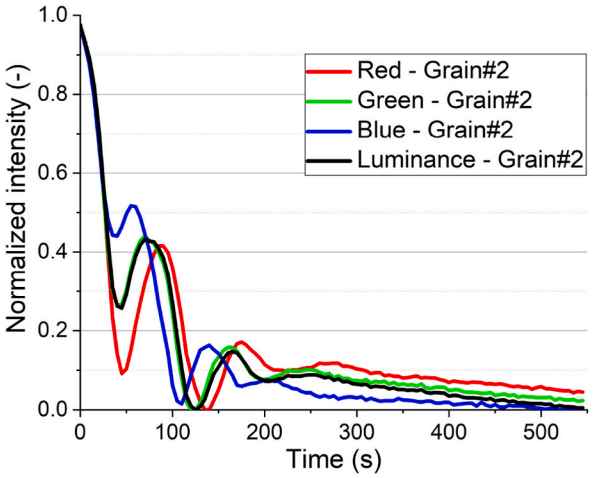


**Fig. 6.** Normalized intensity of grain #2 in the function of time.

the elapsed time between the first local minimum and maximum as in Eq. (4).

$$t_{hc} = t_{max\ 1} - t_{min\ 1} \tag{4}$$

Then, the delay time caused by oxide breakthrough was determined as in Eq. (5):

$$t_{oxide} = t_{min\ 1} - t_{hc} \tag{5}$$

The investigation of observable color change revealed that for the visual differences to appear, a change in the proportion of the components is necessary, as this will result in different colors with various intensities. The moment these intensity curves lose their cosine-like characteristic as the extinction will be too high to distinguish the following extrema, the related luminance will also become quasi-linear. Thus, the onset of over-etching was determined by selecting the moment the luminance curve changes its characteristics [19]. The measured and calculated characteristic times are listed in **Table 2**. Since later, the average of multiple grains over a large area will be investigated, the average critical time values were also calculated for the selected grains. This shows that, as expected, the

**Table 2**
The measured characteristic times in sec for the selected 25 grains at different wavelengths and the calculated half-cycle time ($t_{hc}$), oxide breakthrough time ($t_{oxide}$), and necessary time to reach the over-etched state ($t_{over}$).

| Grain No. | $t_{min1}$ (R) | $t_{max1}$ (R) | $t_{min2}$ (R) | $t_{min1}$ (G) | $t_{max1}$ (G) | $t_{min2}$ (G) | $t_{min1}$ (B) | $t_{max1}$ (B) | $t_{min2}$ (B) | $t_{hc}$ (B) | $t_{oxide}$ (B) | $t_{over}$(B) |
|---|---|---|---|---|---|---|---|---|---|---|---|---|
| 1 | 72 | 130 | 190 | 70 | 115 | 170 | 62 | 103 | 147 | 41 | 21 | 250 |
| 2 | 50 | 87 | 147 | 43 | 70 | 122 | 35 | 57 | 107 | 22 | 13 | 345 |
| 3 | 130 | 220 | 370 | 120 | 200 | 330 | 107 | 167 | 287 | 60 | 47 | n.a |
| 4 | 37 | 70 | 115 | 35 | 55 | 105 | 35 | 45 | 95 | 10 | 25 | 195 |
| 5 | 37 | 70 | 115 | 32 | 55 | 102 | 32 | 45 | 92 | 13 | 19 | 200 |
| 6 | 140 | 255 | 405 | 127 | 225 | 375 | 117 | 182 | 330 | 65 | 52 | n.a |
| 7 | 70 | 120 | 180 | 60 | 110 | 160 | 60 | 80 | 142 | 20 | 40 | 345 |
| 8 | 60 | 110 | 160 | 55 | 87 | 145 | 50 | 70 | 130 | 20 | 30 | 310 |
| 9 | 40 | 75 | 115 | 37 | 60 | 105 | 35 | 50 | 95 | 15 | 20 | 197 |
| 10 | 40 | 70 | 112 | 37 | 55 | 102 | 35 | 47 | 90 | 12 | 23 | 200 |
| 11 | 90 | 170 | 265 | 85 | 155 | 240 | 75 | 125 | 205 | 50 | 25 | 480 |
| 12 | 70 | 132 | 195 | 60 | 115 | 175 | 55 | 90 | 160 | 35 | 20 | 350 |
| 13 | 75 | 145 | 215 | 70 | 130 | 185 | 65 | 105 | 170 | 40 | 25 | 385 |
| 14 | 90 | 165 | 260 | 90 | 147 | 225 | 80 | 120 | 190 | 40 | 40 | 465 |
| 15 | 75 | 135 | 210 | 70 | 115 | 185 | 60 | 95 | 160 | 35 | 25 | 385 |
| 16 | 37 | 62 | 107 | 35 | 50 | 100 | 35 | 45 | 85 | 10 | 25 | 205 |
| 17 | 50 | 80 | 125 | 45 | 65 | 112 | 40 | 55 | 100 | 15 | 25 | 215 |
| 18 | 60 | 115 | 170 | 55 | 100 | 155 | 50 | 75 | 135 | 25 | 25 | 320 |
| 19 | 47 | 87 | 130 | 45 | 70 | 120 | 40 | 60 | 105 | 20 | 20 | 220 |
| 20 | 95 | 165 | 260 | 90 | 152 | 225 | 80 | 120 | 200 | 40 | 40 | 460 |
| 21 | 60 | 110 | 170 | 55 | 92 | 152 | 50 | 70 | 135 | 20 | 30 | 315 |
| 22 | 70 | 130 | 200 | 65 | 110 | 180 | 60 | 80 | 160 | 20 | 40 | 380 |
| 23 | 50 | 95 | 145 | 47 | 75 | 125 | 45 | 62 | 115 | 17 | 28 | 250 |
| 24 | 50 | 95 | 145 | 45 | 85 | 135 | 40 | 65 | 120 | 25 | 15 | 270 |
| 25 | 75 | 135 | 195 | 65 | 115 | 175 | 60 | 100 | 157 | 40 | 20 | 370 |
| Average: | | | | | | | | | | 28 | 28 | 309 |

surface becomes over-etched around 300 s, while the oxide breakthrough requires approx. 28 sec.

Since the exact identification of the examined area is impossible due to the errors of in-situ ellipsometry, the approximate location of interest can be found and evaluated with an optical microscope at proper magnification. As the form and the size of the investigated area with SE are known, an area with the same size and similar shape was also selected on the microscope image. This area is shown with red color in Fig. 5. On the chosen area, the average intensities at different wavelengths were measured. The resulting RGBL normalized intensity curves are shown in Fig. 7 a. They show many similarities compared to what can be obtained from the examination of individual grains. The functions have a cosine-like characteristic with decreasing amplitude, although the decrease has a significantly greater influence compared to the effect on the function of a single grain.

A single grain in low carbon steel etched with Beraha−I usually has three whole cosine periods before the characteristic becomes quasi-linear due to the increased absorption of the layer. While layer interference and absorption together determine the color, as the layer increases and the absorption effect gets more potent, the visible color gets darker and modulates only slightly by interference. Calculating the intensity of a polycrystalline surface means that in every moment, we calculated the average of multiple grains, which in case Fig. 5 at area **A** is over 300, and in case of area **B** is over 70. At the beginning of the etching process, while grains develop their first colors, this average will behave similarly to a single-grain system as a global decrease in intensity occurs. After the intensity of grains with the highest etching speed – i.e., for ferrite grains with <100> orientation – reaching their first minima and their functions start to increase, the average intensity at every wavelength will be the sum of various tendencies. This results in much more flattened curves with fewer and less noticeable extrema.

Although the characteristics are similar, the difference still raises the question of how reliable the chosen area is for comparing it with SE. To answer this question, a second independent area was selected and evaluated, which had a different size and contained completely different grains. The second area is shown with turquoise in Fig. 5, while its intensity curves are shown in Fig. 7 b. The comparison of Fig. 7a and Fig. 7 b shows that the functions are almost identical (Fig. 7c). Although the curves may not move in perfectly the same way, their values at the critical points – which are the extrema – are the same. It is also important to mention that by increasing the size of the evaluated area, the extrema may be better visualized as the effect of the weight resulting from the texture decreases. Consequently, as long as the sampling size is significantly bigger than the average grain size in a homogeneous material, the resulting functions used for the evaluation can be considered the same regardless of the place of observation.

Comparing the characteristic times of the individual grains with the average intensity curve also showed that the over-etching occurs after the first local maximum. Thus, to avoid over-etching, stopping the process before the intensity curve reaches its first maximum is preferable. Unfortunately, the effect of oxide breakthrough cannot be eliminated this way. Nevertheless, it is sure that around 30 s, the steady-state etching must be started, and after the first minimum, it has absolutely no effect. In summary, it is preferred to stop the process between the first two extrema to see the effect of steady-state etching.

### 3.2. *Evaluation of in-situ spectroscopic ellipsometry data*

SE requires an optical model to calculate $\Psi$ and $\Delta$ spectra, and to fit the parameters of the model to have a good agreement between the measured and the calculated spectra. The model used for the in-situ characterization consisted of the metal substrate, the developed layer, and the etching solvent as the ambient from which the light accesses the surface. The optical properties of the substrate have been fitted using the measurement at the initial state of the sample without an overlayer. Then the dielectric function of the substrate has not been fitted during the etching process, only the dispersion of the layer. The dispersions have been described and fitted backward in time using the B-spline method [20]. This approach gains increasing interest [21,22] since it is capable of modeling complex materials with unknown band structures and related dielectric functions, the parameterization of which is usually challenging in a broad spectral range [23,24]. In the B-spline model, the dispersion is described by connected polynomials with adjustable node distance. In turn, the quality of the fitted spectra is described by the mean square error (MSE), which is a weighted sum of squared differences between the measured and calculated $\Psi$ and $\Delta$ values for all the wavelengths [25]. The smaller the value, the better the agreement between the measured and the calculated spectra. MSE below 15 is considered to be a good fit, thus, our model is a highly

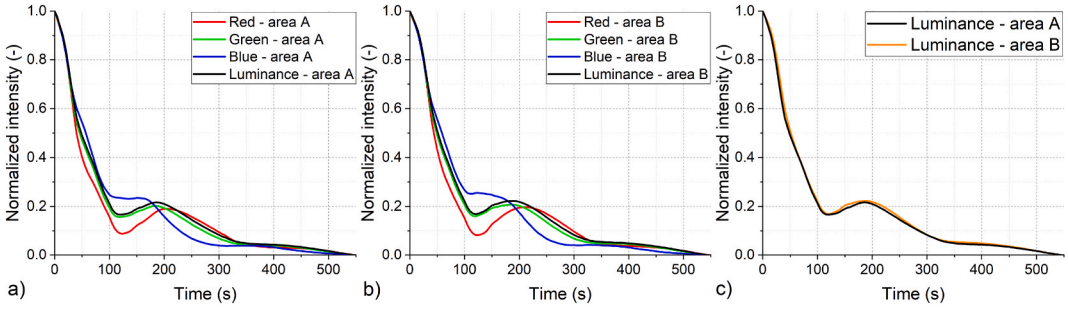


**Fig. 7.** Normalized intensity change of different RGBL components as a function of time from the recorded optical microscope images. The areas on which the average intensity curves were evaluated are shown in Fig. 5 with red (A) and turquoise (B), while the comparison of the luminance curves is shown in (c). (For interpretation of the references to color in this figure legend, the reader is referred to the Web version of this article.)

accurate approximation of the real process, even after the etching was stopped (Fig. 8a). The variations of the MSE below 120 s show an evolving structure in which the accuracy of the model changes substantially, followed by saturation in value between 7 and 8 at the end of the etching.

From the fitted model, the layer thickness was determined (Fig. 8b). First, a constant increase occurs up to a thickness of almost 170 nm. After 120 s, however, a slight but continuous decrease starts. This indicates that the flow rate was increased to flush out the etchant. Unfortunately, though, this resulted in the continuous detachment of the layer's not yet stabilized parts. Although in terms of layer development, this might be unfavorable, it can be utilized to determine the end of the etching process. As a result, in each following figure, the end of the etching will be marked by a purple line.

The luminance change in Fig. 8 c shows that the measurement stopped at the designated intensity range right after the first minimum but before the curve could have reached its first maximum. Consequently, the surface should not be over-etched yet, and the effect of diffusion must be minimal. This, combined with the linear growth in the layer thickness diagram, proves previous hypotheses about the existence of the steady-state etching rate right after the oxide layer was broken through.

By analyzing the refractive index ($n$) and extinction coefficient ($\kappa$) determined by in-situ SE, a similar fluctuation can be observed in Fig. 9, as seen earlier for MSE. These values were calculated from a B-Spline fit that uses a node separation of 0.03 eV by selecting the corresponding point of the spectrum for the temporal behavior. Initially, the refractive index changed as earlier expected, meaning its value decreased as the layer grew. The refractive indices saturated at a value between 1.4 and 1.5 at the wavelength of 600 nm and between 1.3 and 1.4 for the wavelengths of 445 and 540 nm. This range of the red component is very similar to those measured in previous experiments for coarse-grained low-carbon steel with ex-situ ellipsometry, with the difference that this time, not only the final values are known, but the entire course of the change was monitored [13]. Around 50 s, however, not only the direction of the curves but the relative position of the components to one another also changed.

To understand this phenomenon, the layer's absorption must be investigated. The decrease in measured light intensity can be attributed to the increased extinction coefficient of the layer, as the layer interference and extinction determine the color of the individual grains together. If the interference is more dominant, the layer can be considered transparent, and so a cyclic color change can be observed. If the latter is more potent, the layer develops a color that is only slightly modulated by the interference.

In an ideal film with a purely real refractive index ($n$), the interference criteria (Eqs. (1) and (2)) connect the thickness and refractive index of the developed film to the wavelength of the incident light. This means that at a fulfilled wavelength where $cos(\varphi)$ is considered to be 1, the $n \bullet d$ product should theoretically be the same for all grains. However, if at these local extrema, the normalized intensity significantly differs for the various grains (as in many cases occur), the complex refractive index of the layer ($\overline{n}$) has a significant contribution from the extinction coefficient (κ). Thus, the complex nature of the refractive index can be described as in Eq. (6).

$$\overline{n} = n - i\kappa \tag{6}$$

For the individual ferrite grains, the effect of extinction was almost negligible. Even if a significant intensity drop would occur (which mostly did not happen), only the time required to reach certain extrema was utilized, and thus, its influence was eliminated. For the investigation of a whole surface with multiple grains, however, the huge drop in average intensity indicates that it might be a factor to be considered. Fortunately, the fitting function for SE is independent of layer thickness while simultaneously utilizing the refractive index and the extinction coefficient. Thus, the determination of the closely related penetration depth ($d_{pen}$) to $\kappa$ is possible [26,27]. Penetration depth defines the measure of how deep a certain light component can penetrate a medium and is calculated as in Eq. (7).

$$d_{pen}(\lambda) = \frac{\lambda}{4 \bullet \pi \bullet \kappa(\lambda)} \tag{7}$$

It is important to highlight that a given penetration depth does not necessarily mean that light cannot be reflected from below that distance, but its measured intensity will drop to 1/e compared to the original signal. Hence, if the layer thickness overpasses this for a given wavelength, a significant increase in uncertainty occurs [28]. The calculated penetration depth for different wavelengths along the layer thickness is presented in Fig. 10.

After leaving the transition range (52–60 s) and the layer thickness surpasses the penetration depth for the last light component, the error of layer thickness starts a moderate growth. At the end of the etching, this begins to increase drastically since the fitting model was designed for Beraha–I rather than distilled water, which results in an unexpected change in reflection characteristics. Later, when

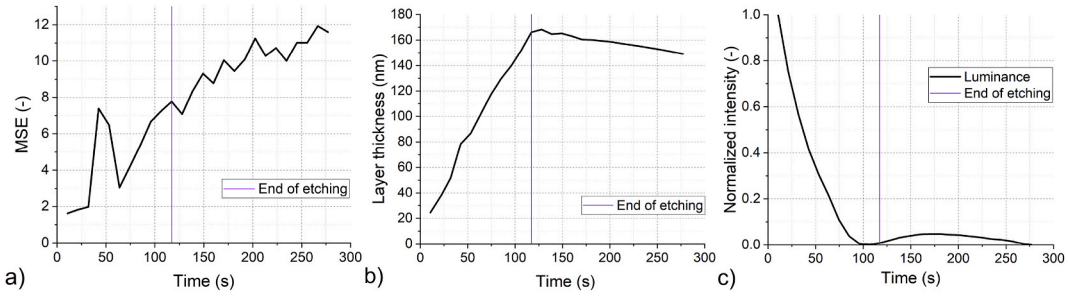


**Fig. 8.** Layer thickness (a) and normalized intensity (b) change during in-situ SE measurement.

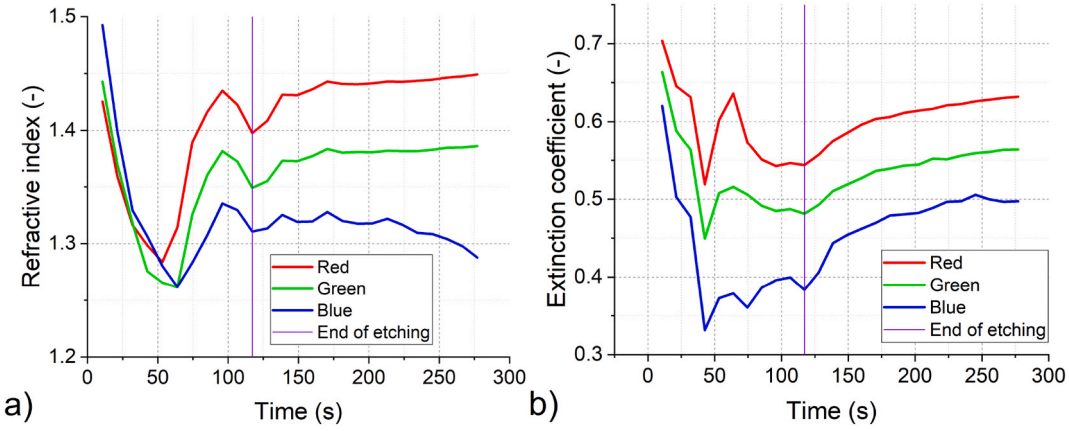


**Fig. 9.** The average refractive indices (a) and extinction coefficients (b) at the wavelengths of 445 (Blue), 540 (Green), and 600 nm (Red), determined by SE. (For interpretation of the references to color in this figure legend, the reader is referred to the Web version of this article.)

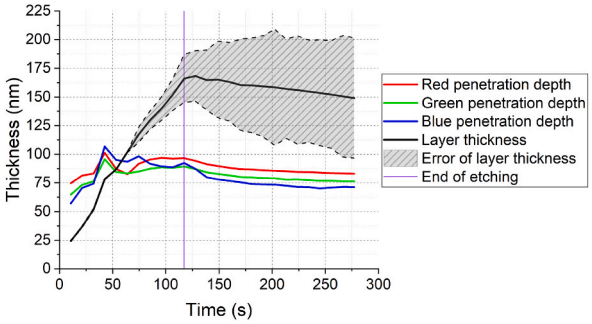


**Fig. 10.** Relation of the penetration depth for RGB components and the measured layer thickness
After the layer became thicker than the penetration depths, the error of thickness began to grow.

the etchant was completely flushed out of the system, the increment of error started to stagnate as well. Although the magnitude of error for layer thickness might be alarming at certain points, the determined values should be considered reliable because the error (along MSE) starts to stagnate at the end of the process instead of starting a drastic increase towards infinity. Consequently, the surface of the substrate (and thus the whole layer) is still visible despite the increased uncertainty.

Additionally, as the magnitude of layer thickness and penetration depth becomes comparable, significant changes occur in the refractive index. As earlier presented, the layer is inhomogeneous, hence, if the layer thickens, its iron concentration decreases in the upper regions, ultimately resulting in a smaller average refractive index. Prior to the transition range, the decrease in the refractive indices of different wavelengths is almost identical, because each observed wavelength can penetrate through the whole layer. Thus, the relative position of the curves fulfills the Cauchy dispersion, meaning that longer wavelengths have smaller refractive index at any given moment. After leaving the transition range, however, the relative positions of the refractive indices change. Shorter wavelengths (i.e., blue) with smaller penetration depths will show smaller refractive indices as they represent only regions close to the surface (with a lower refractive index). Longer wavelengths (i.e., red), on the other hand, penetrate deeper into the layer, resulting in a bigger refractive index as the iron concentration of the lower regions is higher.

This phenomenon proves that the number of free charge carriers in the layer is decreasing during etching because the extinction should increase towards the blue component in metallic materials and increase towards the longer wavelengths (like red) in dielectrics. As a result, this also supports the previous inverstigations which proved that the chemical composition of the layer during the etching process is inhomogeneous, and it changes as the layer grows [13,29].

### *3.3. Comparison of directly and indirectly measured etching rates*

Since not only the layer development rate but also the refractive index is heavily dependent on the orientation, the etching rate alone may not be sufficient to properly describe orientation as earlier assumed because the corresponding refractive index must also be considered. Thus, the $n \bullet d$ product (which includes both orientation-dependent terms) was calculated for each measurement point and presented in Fig. 11 a. Unfortunately, the direct measurement of layer thickness is only available with spectroscopic ellipsometry,

hence, the determination of the same parameter for optical microscope results required another approach. By rearranging Eqs. (1) and (2), the $n \bullet d$ product can be expressed with $\lambda$, $cos(\varphi)$, and $m$, for both constructive and destructive interference. Additionally, $cos(\varphi) = 1$ at each extremum, and the value of $m$ depends on the order of interference that is also known. Thus, the desired product can be calculated for these extrema. Using the RGB components in Fig. 7 a, $n \bullet d$ was calculated for three points, as seen in Fig. 11 b. Although the number of points may not be enough to describe the whole process step by step, they are very good indicators for their corresponding domains.

Since $n \bullet d$ was presented as a function in time for both cases, to determine the etching rate, the derivate of these curves must be calculated, as in Eq. (8). This equation highlights that the etching rate alone cannot be expressed, as the refractive index is also time-dependent, and its derivate must be considered too. To investigate its influence, the partial derivates were also calculated by differentiating the refractive index and layer thickness values in Fig. 8b and Fig. 9 a.

$$\frac{\partial(n(t) \bullet d(t))}{\partial t} = v(t) \bullet n(t) + d(t) \bullet \frac{\partial n(t)}{\partial t} \tag{8}$$

For the OM results, the determination of the $\frac{\partial(n \bullet d)}{\partial t}$ derivate is trivial, as only the slope must be measured between three points. For in-situ SE results, however, the derivate was determined for the whole etching process (between 10−115 s). This calculation is further complicated as each term of the partial derivate is time-dependent, and some of them, like the derivates of the refractive indices (as seen in Fig. 9a), are even changed from positive to negative during the investigation. To eliminate their effects, all terms of the derivates were calculated as a function in time for each measured point. Fig. 12 presents the derivate functions for the blue component.

By analyzing these functions, the $v \bullet n$ and the $\frac{\partial(n \bullet d)}{\partial t}$ values move in relatively tight ranges during the etching process, only a small outlier can be observed around 45 s, where the error of the fitting model was a little higher, probably due to noise in the measurement. These more or less constant values are also expected as Fig. 8b and Fig. 10 show a linear growth in the first 115 s. Additionally, these curves help visualize the slow but steady layer detachment right after the etching stopped. From these functions, the average derivates were determined for the steady etching state. The calculated values are presented in **Table 3**.

Based on these average values, the $v \bullet n$ term has a major influence on the $\frac{\partial(n \bullet d)}{\partial t}$ derivate, as it is significantly larger than $d \bullet \frac{\partial n}{\partial t}$. The difference is so significant that the second partial derivate's absolute value is almost negligible but always less than 3 % of what was observed for $v \bullet n$. Moreover, the $d \bullet \frac{\partial n}{\partial t}$ derivate changes from negative to positive around 45 s, thus, the error of the average value determined as earlier would be higher. Hence, the average values for $d \bullet \frac{\partial n}{\partial t}$ were determined by subtracting $v \bullet n$ from $\frac{\partial(n \bullet d)}{\partial t}$, as it should be the reasonably more accurate method.

As seen in **Table 2** for OM, most grains required less than 25 s to break through the oxide layer, while some needed even less than 15 s. For the initially hydrated sample in SE, this time must be significantly shorter due to the poor corrosion resistance of DC01. Consequently, the derivate determined for the 10−115 s interval is most likely the steady etching state. This statement is also supported by the intensity curve of the whole surface (Fig. 8c) because it barely left its first minimum, and hence, the process did not reach the diffusion-limited domain yet. That is why the layer thickness growth is almost linear in Fig. 8 b. Thus, by knowing that the time interval between $t_{min\ 1}$ and $t_{max\ 1}$ should also be considered as the steady etching state, the OM and the SE results become comparable.

The comparison of the calculated $\frac{\partial(n \bullet d)}{\partial t}$ derivates show multiple similarities. Regardless of the method utilized, the resulting values are very close to one another. Their average value is 1.90 nm/s for DC01 during the steady-state etching with a deviation of ±0.15 nm/s.

Moreover, for OM, a second time interval was also calculated between $t_{max\ 1}$ and $t_{max\ 2}$. Considering that $t_{max\ 2} = 430\ s$ for the red component here, the domain between $t_{max\ 1}$ and $t_{max\ 2}$ must contain large over-etched areas, where the etching rate has already begun to decrease. The measurements show an obvious decrease in the etching rate compared to the earlier stages, indicating the continuously increasing effect of diffusion as the process develops. Here, the average of the derivates was 1.67 ± 0.03 nm/s, showing a large

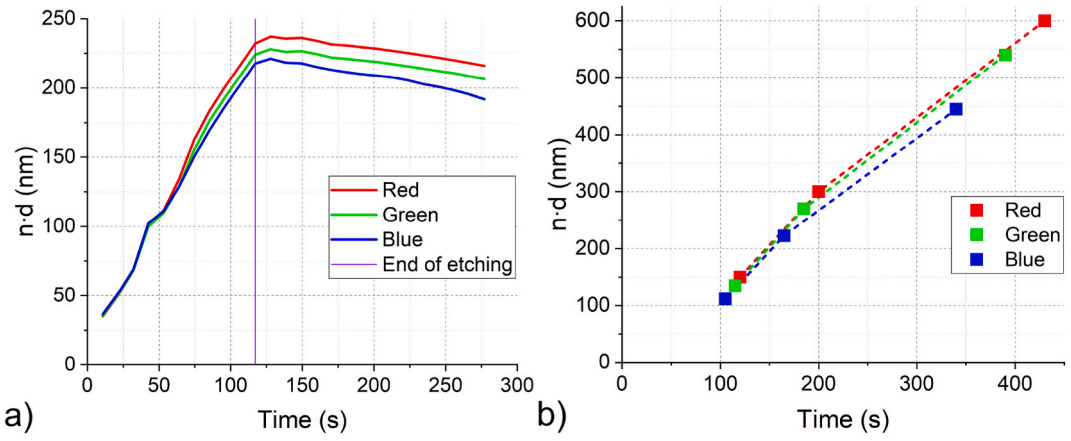


**Fig. 11.** Comparison of the $n \bullet d$ product calculated for DC01 with SE (a) and OM(b) analysis.

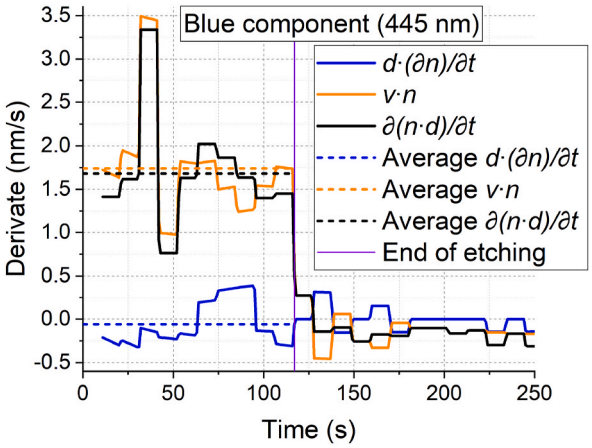


**Fig. 12.** Derivates of the blue component as a function in time based on SE measurements. (For interpretation of the references to color in this figure legend, the reader is referred to the Web version of this article.)

**Table 3**
The $n \bullet d$ derivate of RGB wavelengths in different domains for OM and SE.

| Examination type | Domain | Component | Value (nm/s) | | |
|---|---|---|---|---|---|
| | | | R | G | B |
| Spectroscopic Ellipsometry | Steady-state etching (10–115 s) | $v \bullet n$ | 1.80 | 1.81 | 1.79 |
| | | $\frac{\partial(n \bullet d)}{\partial t}$ | 1.85 | 1.77 | 1.70 |
| Optical Microscopy | Steady-state etching (between $t_{min\ 1}$ and $t_{max\ 1}$) | $\frac{\partial(n \bullet d)}{\partial t}$ | 2.00 | 2.08 | 2.02 |
| | Diffusion limited etching (between $t_{max\ 1}$ and $t_{max\ 2}$) | | 1.65 | 1.70 | 1.65 |

drop compared to what was calculated for the domain of the steady-state etching.

### 3.4. Etching rate of the ferrite phase in different materials

In our previous works, the average etching rate and the refractive indices were determined for ferrite in spheroidal graphite cast iron with the microfluidic cell presented in Fig. 2, although at that time, the functional kinetics model based on the optical microscope and the atomic force microscope was used instead of SE [11,30]. The ferrite phase in both materials are being etched very similarly, in cast iron, however, the process took much longer. To compare these etching rates (and $\frac{\partial(n \bullet d)}{\partial t}$, considering that it gives a much more comprehensive picture of the ongoing process), cast iron was also color etched to determine the yet missing extrema of the average intensity curves. The color etched spheroidal graphite cast iron surface can be seen in Fig. 13 a.

Since the etching rate and refractive index was determined exclusively for ferrite earlier, only the average intensity-change of the individual ferrite grains must be measured instead of the whole heterogeneous surface. To do so without altering the results due to the influence of pearlite and graphite, the average intensity was calculated for 30 randomly selected grains (Fig. 13a). From the average intensity curves of these grains, later, the characteristic times of the local extrema were determined (Fig. 13b).

Then, based on the so-determined intensity values and the etching rate calculated in the previous works, the $n \bullet d$ products were assigned to discrete time values, similar to Fig. 11 b. The $n \bullet d$ change as a function in time for cast iron is presented in Fig. 14.

A direct comparison between ferrite in cast iron and low-carbon steel shows that compared to DC01, cast iron is etched significantly slower. While it was very hard to identify the second local minimum on the average intensity curves for low-carbon steel, it was relatively easy to find it for cast iron. Due to the slower etching rate, however, the second local maximum could not be found, as the process did not reach it during the observation.

Since the $n \bullet d$ product shows no decrease in the slope, and the increment looks more or less linear (as their difference is negligible), indicating that for cast iron, even this domain can be considered as the steady etching state. Consequently, its investigation may not result in new conclusions, thus, only the first interval must be investigated in depth. The average layer buildup rate, refractive indices, and other calculated values for cast iron are shown in **Table 4**.

Similarly to previous observations, the $v \bullet n$ product will mostly influence the value of the derivate, while the influence of $d \bullet \frac{\partial n}{\partial t}$ is only around 5 %. Additionally, the $\frac{\partial(n \bullet d)}{\partial t}$ derivative has an average of $0.99 \pm 0.06$ nm/s, which is approx. half of what was observed for low-carbon steel. This value corresponds well with the expectations since cast iron has significantly better corrosion resistance. In accordance with this, its surface starts becoming over-etched only at around 550 s, which is almost twice as much as low-carbon steel required. Finally, a slower layer buildup rate results in the effect of diffusion appearing later, as the etchant has a longer time to react

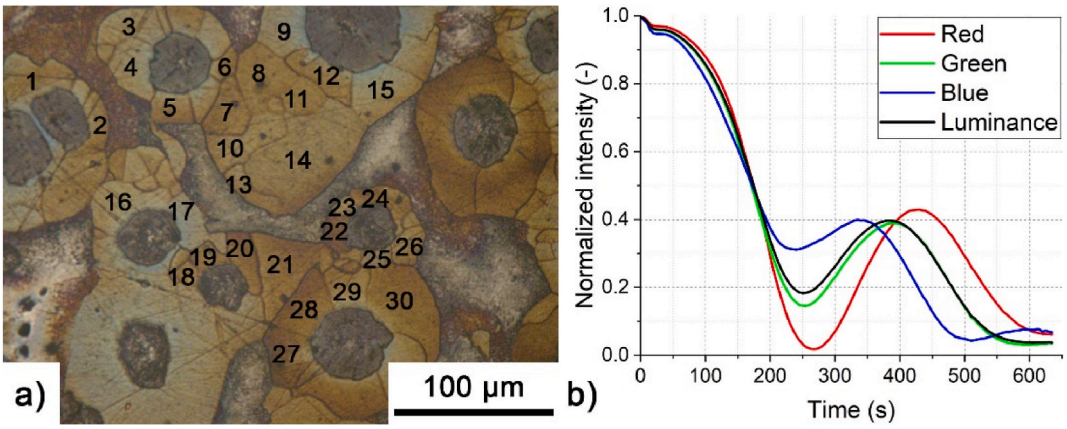


**Fig. 13.** Spheroidal graphite cast iron with the selected 30 ferrite grains (a) and the calculated average intensity curves (b).

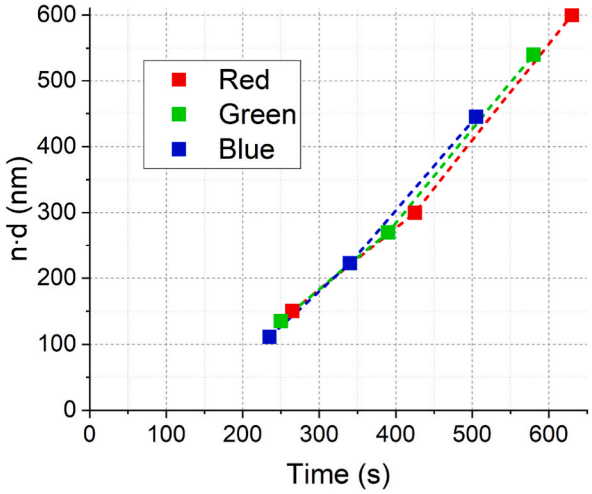


**Fig. 14.** The $n \bullet d$ product calculated for ferrite in spheroidal graphite cast iron with OM analysis.

**Table 4**
The $n \bullet v$ product of RGB wavelengths in different domains for cast iron.

| Examination type | Characteristic value | | Value | | |
|---|---|---|---|---|---|
| | | | R | G | B |
| Optical Microscopy | Etching rate (nm/s) | | 0.49 | | |
| | Refractive index (−) | | 1.81 | 1.92 | 2.22 |
| | **Domain** | **Component** | (nm/s) | (nm/s) | (nm/s) |
| | Steady-state etching (between $t_{min\ 1}$ and $t_{max\ 1}$) | $v \bullet n$ | 0.89 | 0.94 | 1.09 |
| | | $\frac{\partial(n \bullet d)}{\partial t}$ | 0.94 | 0.96 | 1.06 |

with the substrate. That is why the influence of over-etching is negligible between $t_{max\ 1}$ and $t_{min\ 2}$, and why cast iron is required almost twice the time to reach over-etching compared to DC01.

## 4. Conclusions

In summary, first in the world, in-situ color etching observations were performed while the developing layer was monitored with spectroscopic ellipsometry. These observations proved the existence of the previously hypothesized steady-state etching rate in the early phases of the process. This etching rate will later decrease as the diffusion becomes relevant enough to hinder the reaction between the etchant and the substrate. The chemically inhomogeneous nature of the developed layer was also supported by the

addition that not only the refractive index but the extinction coefficient with the related penetration depth will also change as the layer grows. Penetration depth showed that the extinction must also be considered during observations, even if its effect may look negligible for the individual grains. If the penetration depth becomes comparable in size to the layer thickness, the measurement error will increase, which may distort the results.

Finally, the determination of the $\frac{\partial(n \bullet d)}{\partial t}$ derivative showed that for the DC01 material with different microfluidic cells (even if the circumstances may not be perfectly identical, but the etchant flow rate is similarly slow), the derivative that is in close connection to the layer buildup rate could be determined with very high accuracy. According to our measurements, the derivative moved around $1.90 \pm 0.15$ nm/s for the steady-state etching domain and $1.67 \pm 0.03$ nm/s for the observed part of the diffusion-limited domain. By calculating the derivative for cast iron as well, it was shown that the steady-state etching rate is approx. half for ferrite in cast iron due to its better corrosion resistance. In addition to that, the etching rate of cast iron was nearly constant until 550 s, as the derivative between $t_{max\ 1}$ and $t_{min\ 2}$ had negligible differences compared to what was obtained between $t_{min\ 1}$ and $t_{max\ 1}$. For the steady etching state, the $\frac{\partial(n \bullet d)}{\partial t}$ derivative for cast iron was $0.99 \pm 0.06$ nm/s. The determined etching rates thus correlate well with the corrosion resistance of the investigated materials.

## Data availability statement

The data presented in this study are available on request from the corresponding author.

## CRediT authorship contribution statement

**József Bálint Renkó:** Writing – original draft, Investigation. **Alekszej Romanenko:** Investigation. **Tamás Bíró:** Investigation. **Péter János Szabó:** Supervision, Methodology. **Péter Petrik:** Methodology, Investigation, Data curation. **Attila Bonyár:** Writing – review & editing, Writing – original draft, Methodology, Conceptualization.

## Declaration of competing interest

The authors declare the following financial interests/personal relationships which may be considered as potential competing interests:Attila Bonyár reports financial support was provided by National Research Development and Innovation Office. Péter János Szabó reports financial support was provided by National Research Development and Innovation Office. Péter Petrik reports financial support was provided by National Research Development and Innovation Office.. If there are other authors, they declare that they have no known competing financial interests or personal relationships that could have appeared to influence the work reported in this paper.

## Acknowledgments

Project no. TKP-6-6/PALY-2021 has been implemented with the support provided by the Ministry of Culture and Innovation of Hungary from the National Research, Development and Innovation Fund, financed under the TKP2021-NVA funding scheme. Partial support from National Scientific Research Fund OTKA K-146181 is also appreciated. The work in frame of the 20FUN02 ‘‘POLight’’ project has received funding from the EMPIR programme co-financed by the Participating States and from the European Union’s Horizon 2020 research and innovation programme. Project no. TKP2021-EGA04 has been implemented with the support provided by the Ministry of Innovation and Technology of Hungary from the National Research, Development and Innovation Fund, financed under the TKP2021 funding scheme. Attila Bonyár is also grateful for the support of the Hungarian Academy of Engineering and the "MICHELBERGER MESTERDÍJ" Scholarship.

## References

[1] G.F. Vander Voort, Metallography, Principles and Practice, New York McGraw-Hill Book Co., Materials Park, Ohio, 1984. ASM International, https://books.google.hu/books?hl=hu&lr=&id=GRQC8zYqtBIC&oi=fnd&pg=PR12&dq=etching+metallography&ots=_zl-U6AylV&sig=LSbx5Ig_6qxsVrb0mNN8NFc1B28&redir_esc=y#v=onepage&q=etching%20metallography&f=false. (Accessed 3 October 2022).

[2] G. Petzow, Metallographic Etching : Techniques for Metallography, Ceramography, Plastography, second ed., ASM International, Materials Park, Ohio, 1999. . [Online]. Available: https://archive.org/details/metallographicet0000petz/page/n5/mode/2up. (Accessed 18 January 2023).

[3] C. Fleißner-Rieger, et al., An Additively manufactured Titanium alloy in the focus of metallography, Pract. Metallogr. 58 (1) (Jan. 2021) 4–31, https://doi.org/10.1515/PM-2020-0001.

[4] O. Çakır, Review of etchants for copper and its alloys in Wet etching processes, Key Eng. Mater. 364–366 (Dec. 2008) 460–465, https://doi.org/10.4028/WWW.SCIENTIFIC.NET/KEM.364-366.460.

[5] ASM metals Handbook, in: G.F. Vander Voort (Ed.), Vol. 9 Metallography and Microstructures, vol. 9, ASM International, Materials park, Ohio, 1985. . [Online]. Available: https://docs.google.com/file/d/0B3Mrzn2Z7-tSbURmRThQQnh6Skk/edit?resourcekey=0-bWLfD0aUKlQJBs7laEr31Q. (Accessed 18 January 2023).

[6] I. Kardos, Z. Gácsi, Investigation of microstructure of cast iron by color etching, Mater. Sci. Forum 752 (2013) 167–174, https://doi.org/10.4028/WWW.SCIENTIFIC.NET/MSF.752.167.

[7] D. Britz, Y. Steimer, F. Mücklich, A New Approach for Color Metallography: through Controlled Conditions to Objective Microstructure Analysis of Low-Carbon Steels by LePera-Etching, ASTM Special Technical Publication, Apr. 2019, pp. 130–151, https://doi.org/10.1520/STP160720170242, vol. STP 1607.

[8] A. Bonyár, P.J. Szabó, A method for the determination of ferrite grains with a surface normal close to the (111) orientation in cold rolled steel samples with color etching and optical microscopy, Mater. Sci. Forum 812 (2015) 297–302, https://doi.org/10.4028/WWW.SCIENTIFIC.NET/MSF.812.297.

[9] Y. Li, et al., Fabrication of sharp silicon hollow microneedles by deep-reactive ion etching towards minimally invasive diagnostics, Microsyst Nanoeng 5 (1) (Aug. 2019) 1–11, https://doi.org/10.1038/s41378-019-0077-y.

[10] J. Fan, L. Qian, Quantum dot patterning by direct photolithography, Nat. Nanotechnol. 17 (9) (Aug. 2022) 906–907, https://doi.org/10.1038/s41565-022-01187-0, 2022 17:9.
[11] A. Bonyár, J. Renkó, D. Kovács, P.J. Szabó, Understanding the mechanism of Beraha-I type color etching: determination of the orientation dependent etch rate, layer refractive index and a method for quantifying the angle between surface normal and the ⟨100⟩, ⟨111⟩ directions for individual grains, Mater. Char. 156 (2019), https://doi.org/10.1016/j.matchar.2019.109844.
[12] C.J. Van Der Kooi, J.T.M. Elzenga, J. Dijksterhuis, D.G. Stavenga, Functional optics of glossy buttercup flowers, J. R. Soc. Interface 14 (127) (Feb. 2017) 20160933, https://doi.org/10.1098/RSIF.2016.0933.
[13] J.B. Renkó, A. Romanenko, P.J. Szabó, P. Petrik, A. Bonyár, Analysis of the microstructure of color etched low carbon steel with spectroscopic ellipsometry, Symposium on Materials Science 1 (Oct. 2021) 20–24.
[14] G.F. Vander Voort, 'Copper Color Metallography', Advanced Materials & Processes 158 (1) (Jul. 2000) 36, 36, https://go.gale.com/ps/i.do?p=AONE&sw=w&issn=08827958&v=2.1&it=r&id=GALE%7CA63914855&sid=googleScholar&linkaccess=fulltext. (Accessed 24 January 2023).
[15] E. Beraha, Staining metallographic Reagents for cast iron, steels, tool steels, Manganese steels, and ferritic and Martensitic Stainless steel, Prakt. Metallogr. 8 (Sep. 1971) 547.
[16] J.B. Renkó, P.J. Szabó, A. Bonyár, Correlation between the developed layer's color and crystallographic orientation of pure copper during long-term color etching with Beraha−I, J. Mater. Res. Technol. 23 (Mar. 2023) 4346–4354, https://doi.org/10.1016/J.JMRT.2023.02.082.
[17] T. Bíró, J.B. Renkó, Design and manufacture of a microfluidic cell to Be used with a spectroscopic ellipsometer, Acta Materialia Transylvanica 4 (1) (Apr. 2021) 28–31, https://doi.org/10.33924/AMT-2021-01-05.
[18] J. Manzano, D. Filippini, I. Lundström, Computer screen illumination for the characterization of colorimetric assays, Sensor. Actuator. B Chem. 96 (1–2) (Nov. 2003) 173–179, https://doi.org/10.1016/S0925-4005(03)00523-9.
[19] J.B. Renkó, P.J. Szabó, Investigation of the effect of over-etching during color etching, Acta Materialia Transylvanica 5 (1) (Apr. 2022) 29–34, https://doi.org/10.33924/AMT-2022-01-07.
[20] B. Johs, J.S. Hale, Dielectric function representation by B-splines, Phys. Status Solidi 205 (4) (Apr. 2008) 715–719, https://doi.org/10.1002/PSSA.200777754.
[21] D.V. Likhachev, On the optimization of knot allocation for B-spline parameterization of the dielectric function in spectroscopic ellipsometry data analysis, J. Appl. Phys. 129 (3) (Jan. 2021) 034903, https://doi.org/10.1063/5.0035456.
[22] D.V. Likhachev, Certain topics in ellipsometric data modeling with splines: a review of recent developments, Adv. Opt. Technol. 11 (3–4) (Sep. 2022) 93–115, https://doi.org/10.1515/AOT-2022-0006/MACHINEREADABLECITATION/RIS.
[23] P. Petrik, Parameterization of the dielectric function of semiconductor nanocrystals, Phys. B Condens. Matter 453 (Nov. 2014) 2–7, https://doi.org/10.1016/J.PHYSB.2014.03.065.
[24] E. Agocs, et al., Approaches to calculate the dielectric function of ZnO around the band gap, Thin Solid Films 571 (P3) (Nov. 2014) 684–688, https://doi.org/10.1016/J.TSF.2014.03.028.
[25] T. Lohner, M. Serényi, P. Petrik, Characterization of sputtered aluminum oxide films using spectroscopic ellipsometry, International Journal of New Horizons in Physics 2 (1) (2015) 1–4, https://doi.org/10.12785/ijnhp/020101.
[26] X. Ziang, et al., Refractive index and extinction coefficient of CH3NH3PbI3 studied by spectroscopic ellipsometry, Opt. Mater. Express 5 (1) (Jan. 2015) 29–43, https://doi.org/10.1364/OME.5.000029. Vol. 5, Issue 1, pp. 29–43.
[27] S. Del Bianco, F. Martelli, G. Zaccanti, Penetration depth of light re-emitted by a diffusive medium: theoretical and experimental investigation, Phys. Med. Biol. 47 (23) (Nov. 2002) 4131, https://doi.org/10.1088/0031-9155/47/23/301.
[28] A. Douplik, G. Saiko, I. Schelkanova, V.V. Tuchin, 'The response of tissue to laser light', Lasers for Medical Applications: diagnostics, Therapy and Surgery (Jan. 2013) 47–109, https://doi.org/10.1533/9780857097545.1.47.
[29] J.B. Renkó, A. Romanenko, P.J. Szabó, A. Sulyok, P. Petrik, A. Bonyár, Analysis of structural and chemical inhomogeneity of thin films developed on ferrite grains by color etching with Beraha-I type etchant with spectroscopic ellipsometry and XPS, J. Mater. Res. Technol. 18 (May 2022) 2822–2830, https://doi.org/10.1016/J.JMRT.2022.03.159.
[30] J.B. Renkó, A. Bonyár, P.J. Szabó, Effect of Beracha-I type color etchant on the ferrite phase in different type Fe-C alloys, IOP Conf. Ser. Mater. Sci. Eng. 903 (1) (Aug. 2020) 012054, https://doi.org/10.1088/1757-899X/903/1/012054.